ACS APPLIED MATERIALS & INTERFACES

Functional Inorganic Materials and Devices

Targeted nanoparticles for selective marking of neuromuscular junctions and ex vivo monitoring of endogenous acetylcholine hydrolysis

Alsu R. Mukhametshina, Svetlana V. Fedorenko, Alexey M. Petrov, Guzel F. Zakyrjanova, Konstantin A. Petrov, Leniz F. Nurullin, Irek R. Nizameev, Asiya R. Mustafina, and Oleg G. Sinyashin

ACS Appl. Mater. Interfaces, **Just Accepted Manuscript** • DOI: 10.1021/acsami.8b04471 • Publication Date (Web): 13 Apr 2018

ACS Publications

is published by the American Chemical Society. 1155 Sixteenth Street N.W., Washington, DC 20036

Targeted nanoparticles for selective marking of neuromuscular junctions and *ex vivo* monitoring of endogenous acetylcholine hydrolysis

Alsu R. Mukhametshina[1,], Svetlana V. Fedorenko[1], Alexey M. Petrov[2,3], Guzel F. Zakyrjanova[3], Konstantin A. Petrov[1], Leniz F. Nurullin[3], Irek R. Nizameev[1], Asiya R. Mustafina[1], Oleg G. Sinyashin[1]*

[1]Arbuzov Institute of Organic and Physical Chemistry, FRC Kazan Scientific Center of RAS, Arbuzov Str. 8, 420088 Kazan, Russian Federation

[2]Kazan State Medial University, Butlerov Str. 49, 420012 Kazan, Russian Federation

[3]Kazan Institute of Biochemistry and Biophysics, Federal Research Center "Kazan Scientific Center of RAS", P.O. box 30, 420111 Kazan, Russian Federation

KEYWORDS

Synapse, endogenous acetylcholine, Tb(III) complex, *ex vivo* sensing, luminescence

ABSTRACT

The present work for the first time introduces nanosensors for luminescent monitoring of acetylcholinesterase (AChE)-catalyzed hydrolysis of endogenous acetylcholine (ACh) released in neuromuscular junctions of isolated muscles. The sensing function results from the quenching of Tb(III)-centered luminescence due to proton-induced degradation of luminescent Tb(III) complexes doped into silica nanoparticles (SNs, 23 nm), when acetic acid is produced from the enzymatic hydrolysis of ACh. The targeting of the silica nanoparticles by α-bungarotoxin was used for selective staining of the synaptic space in the isolated muscles by the nanosensors. The targeting procedure was optimized for the high sensing sensitivity. The measuring of the Tb(III)-centered luminescence intensity of the targeted SNs by fluorescent microscopy enables to sense a release of endogenous ACh in neuromuscular junctions of the isolated muscles under their stimulation by high-frequency train (20Hz, for 3 min). The ability of the targeted SNs to sense an inhibiting effect of paraoxon on enzymatic activity of AChE in *ex vivo* conditions provides a way of mimicking external stimuli effects on enzymatic processes in the isolated muscles.

INTRODUCTION

Motor neurons make contact with muscles at specialized sites called neuromuscular junctions. Failing to send the correct signals to the muscles at these junctions can lead to muscle fatigue and even death if the respiratory muscles are unable to contract. Studying of neuromuscular synaptic transmission in *ex vivo* conditions can provide deeper insight into reasons for neurological and neuromuscular disorders and ways of their treatment.[1] Thus, *ex vivo* monitoring of endogenous acetylcholine (ACh), which is the neurotransmitter that triggers contraction of skeletal muscle cells, is very challenging task. The majority of techniques available from literature are based on electrochemical or fluorescent enzyme-based assays paired with microdialysis of ACh.[2-15] Main limitation of microdialysis is an off-line sample analysis, which results in long sampling interval from 5 to 20 minutes.[1,2,7-11] This precludes simultaneous monitoring of dynamic changes in concentration of endogenous ACh.

The space between the motor nerve terminal and the postsynaptic membrane, the synaptic cleft, is about 50 nm, it is much smaller than microelectrodes applied in current technologies for monitoring of the neurotransmitter.[7–11] Thus, microelectrode-based probes are unable to access a single synapse due the size limitations, which has become the reason for development of nanoscale sensors for visualizing dynamic changes in ACh concentration in synaptic cleft or very close to it. It is worth noting that nanosized sensors for efficient *ex vivo* monitoring of ACh[15,16] are insufficiently reported in literature. Moreover, the literature data represent the techniques based on multicomponent nanodevices containing the two different enzymes.[15,16] Thus, a development of low-cost nanosensors able to visualize the enzymatic hydrolysis taking part in synaptic clefts is still challenging task.

Our previous articles are worth noting as convenient basis for the sensor, where the sensing function results from the quenching of terbium(III)-centered luminescence by H^+ ions produced by the AChE-catalyzed hydrolysis of ACh.[17,18] The Tb(III)-centered luminescence, in turn, derives from Tb(III) complexes with p-sulfonatothiacalix[4]arene tetrasodium salt ([Tb(TCAS)]) embedded into silica nanoparticles.[19] The embedding of the complexes into silica nanoparticles restricts their deliverance from the nanosensors,[19] while the Tb(III) complexes inside silica nanoparticles (SNs) are still accessible for H^+ ions which is illustrated by Scheme 1. This, in turn, minimizes both the inhibiting effect of Tb(III) ions on the activity of AChE[17] and cytotoxicity of the nanoparticles.[20] The size of the Tb-doped SNs should be minimized for the high sensitivity of the SNs to H^+ ions.[17,18] In particular, the Tb-doped SNs with the size about 20 nm were enough sensitive for *in vitro* monitoring of AChE-catalyzed hydrolysis of ACh.[18] Nevertheless, monitoring of the enzymatic hydrolysis in neuromuscular junctions requires specific targeting of the SNs. The targeting by α-bungarotoxin (α-BGT) is promising route of gaining in affinity of the SNs to synaptic region, since the commercially available dye-labeled α-bungarotoxin is widely applied in the staining of neuromuscular junctions.

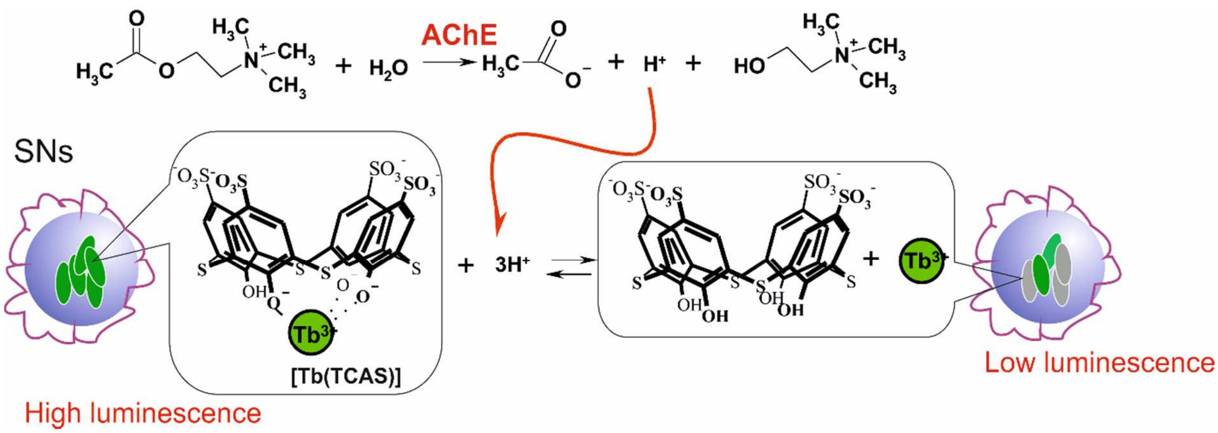

Scheme 1. Schematic presentation of AChE-catalyzed hydrolysis of ACh and its sensing through the luminescence of Tb(III) complexes.

Thus, the present work introduces the targeting of the Tb-doped SNs by α-BGT as a way of selective staining of synaptic clefts in frog cutaneous pectoris muscle. The sensing function of the targeted SNs is revealed herein in both *in vitro* and *ex vivo* conditions, thus, resulting in development of the optimal nanosensors for monitoring of the enzymatic hydrolysis at the neuromuscular junctions.

RESULTS AND DISCUSSION

As it has been above mentioned development of the *ex vivo* sensor is based on previously reported Tb(III)-doped SNs with the size about 20 nm, which should be properly targeted for their selective localization in neuromuscular junctions. Presentation of the data concerning an optimization of a targeting procedure should be preceded by discussion of main factors affecting the sensitivity of the nanosensors to acetic acid. It is worth noting that the higher sensitivity of these SNs versus the greater in size (35 nm) SNs results from the predominant surface localization of the luminescent Tb(III) complexes in the smaller versus larger nanoparticles.[17,18] However, the higher surface activity of the smaller (~20 nm) SNs versus the larger (35 nm) ones is the reason for the aggregation-induced quenching, which has been previously reported for the smaller SNs under their surface decoration by amino-groups.[20] Moreover, the aggregation is the reason for decreased active surface of the SNs. This, in turn, can be a reason for smaller sensitivity to acetic acid. Thus, the aggregation of the SNs should be minimized under their targeting by α-BGT. The surface decoration of the SNs by amino-groups is worth noting as one more factor decreasing the sensitivity of the nanosensor. In particular, it was previously revealed[17] that the average number of amino-groups about 3000 per SN is the reason for poor sensitivity of Tb(III)-centered luminescence of the complexes inside the SNs (~35 nm) to acetic acid, while the sensitivity of the smaller (~20 nm) SNs is enough when they are decorated by ~300 amino-groups per SN.[18] Targeting of silica nanoparticles by proteins requires their surface modification by amino-groups with their following conversion into aldehyde- or carboxy-groups. Thus, both the number of residual amino-groups and aggregation of the decorated SNs should be monitored and controlled in the synthesis of the nanosensor.

Targeting of Tb(III)-doped silica nanoparticles by α-BGT

Targeting of silica nanoparticles by peptides is commonly performed through preliminary silica surface decoration by aldehyde- or carboxy-groups.[21-29] The both decoration procedures represented in Figure 1 were applied in the targeting of the SNs by α-bungarotoxin in order to choose the optimal one for the higher sensitivity of the nanosensor to acetic acid. The first decoration mode[21-29] is based on a transformation of amino- to aldehyde- groups via interaction with glutaraldehyde, while the second one[30-42] is based on conversion of amino- to carboxy-groups through the reaction with succinic anhydride. Both types of the SNs decorated by aldehyde- or carboxy-groups were further bioconjugated with α-BGT.

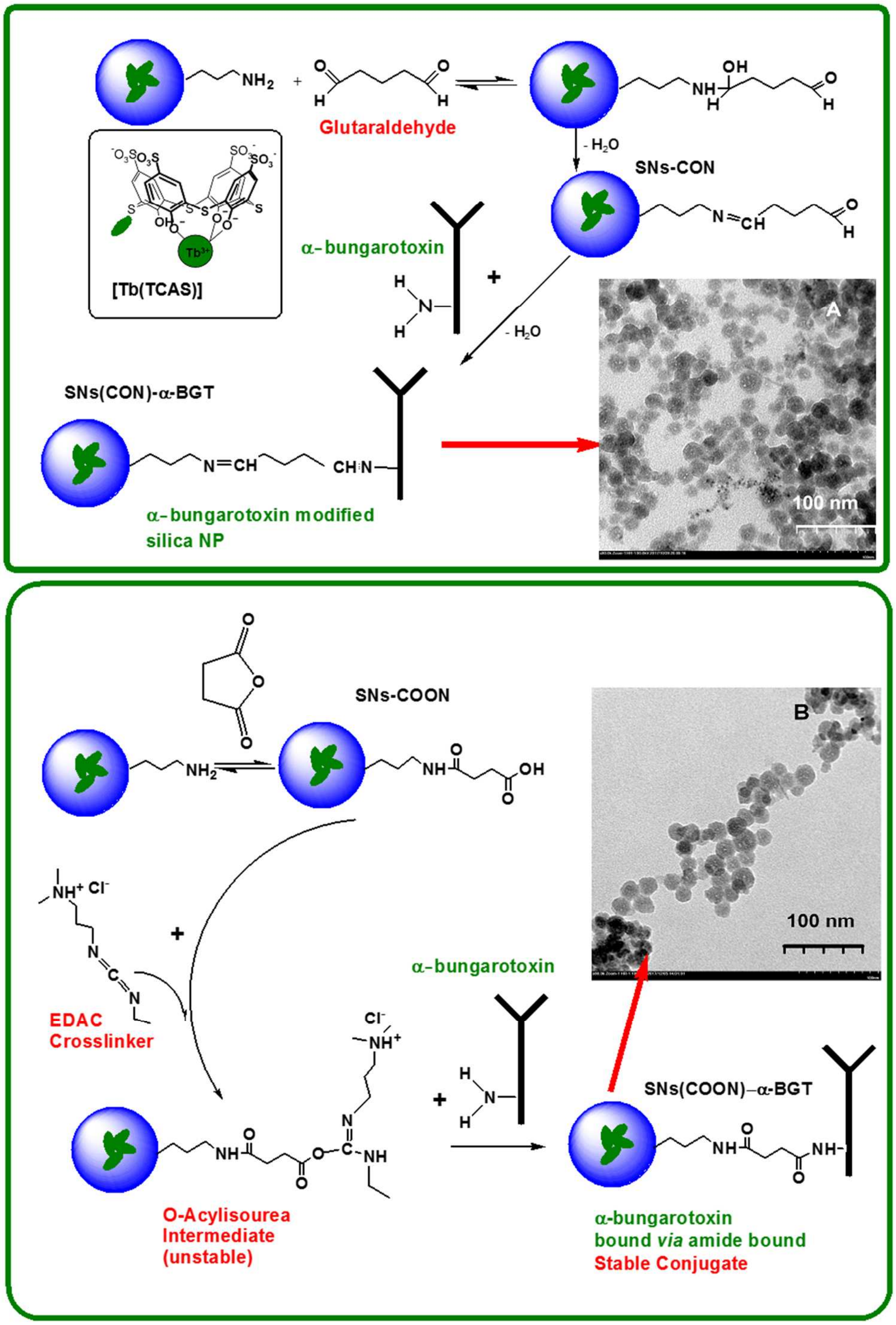

Figure 1. Schematically presented synthetic routes of the silica surface modification for the targeting by α-bungarotoxin and TEM images of the targeted nanoparticles.

The both surface decoration procedures were started from initial luminescent amino-decorated nanoparticles (SNs-NH_2, 23±3 nm). Taking into account the above mentioned impact of the amino-decoration on sensing and colloid properties of the SNs the synthetic procedure was modified with the aim to decorate the nanoparticles by smaller amount (1283±5) of amino-groups per nanoparticle (for more details see Experimental Section in Supporting Information (SI)).

Each step of the decoration procedures was followed by a quantitative analysis of a decoration extent. Quantitative evaluation of residual amino-groups after their transformation to aldehyde- or carboxy-groups was performed by means of fluorescamine procedure[43] with further calculation of the corresponding transformation extents (Fig. S1 in SI). Thus, the average number of residual amino-groups was about 435 and 115 when the amino-groups were transformed into aldehyde- and carboxy-groups correspondingly. Thus, calculated transformation extent of amino-groups is higher (91%) for carboxy-decorated (SNs-COOH) nanoparticles versus 66% for the aldehyde-decorated ones (SNs-COH). The TEM images of the aldehyde- (SNs-COH) and carboxy-decorated (SNs-COOH) nanoparticles reveal no difference between them, which is rather anticipated (Fig.S2 in SI).

Table 1. Averaged size (D), electrokinetic potential (ζ) values and polydispersity indices (PDI) from DLS measurements in aqueous solutions for different type of SNs, where $C_{SNs} = 0.05$ g·L^{-1}.

Type of SNs	**D, nm**	**PDI**	**ζ, мВ**
SNs-NH_2	*aggregation*	0.94	+19±1
SNs-COOH	406±23	0.41	-37±1
SNs(COOH)-α-BGT	202±2	0.20	-34±1
SNs-COH	*aggregation*	1	-15±5

SNs(COH)-α-BGT	*aggregation*	0.91	-25±5

The aggregation of amino-decorated SNs is rather high (Table 1). Their transformation into SNs-COH remains the aggregation on the high level, while the transformation of amino- to carboxy-groups results in significant de-aggregation of the nanoparticles (Table 1). The aggregation behavior of the SNs is in good agreement with electrokinetic potential values (ζ) measured in aqueous colloids of the SNs (Table 1). The ζ value is about +19 mV for the initial amino-decorated SNs (SNs-NH_2) nanoparticles, while the ζ values after the conversion of the amino- to carboxy- (SNs-COOH) and aldehyde-groups (SNs-COH) are about -37 mV and -15 mV correspondingly (Table 1). Thus, the greater size (d) and polydispersity index (PDI) values measured for SNs-COH versus SNs-COOH are in good agreement with the ζ values (Table 1). Moreover, literature data[21] are worth noting for highlighting interparticle cross-linking ability of glutaraldehyde which also can be a reason for the greater aggregation of SNs-COH versus SNs-COOH.

The bioconjugation of both SNs-COH and SNs-COOH with α-BGT results in insignificant changes in the TEM images of the targeted nanoparticles (Figs.1 A, B). The DLS measurements (Table 1) indicate some decrease in the aggregation behavior of the targeted SNs-COOH, while the aggregation behavior remains on the high level for SNs-COH after their targeting.

The fluorescamine-based fluorescence procedure is the convenient tool for accurate quantitative analysis of amino-decoration of nanoparticles, moreover this procedure is low concentration consuming.[43,44] Taking into account that amino-groups of α-BGT are well visualized by the fluorescamine-based procedure (Figs. S3 a, b), the latter was applied to compare the quantity of α-BGT deposited onto SNs-COH and SNs-COOH. The contribution of the residual amino-groups in SNs-COOH and SNs-COH colloids to the fluorescence of fluorescamine was taken into account in the comparative quantitative analysis of the differently targeted nanoparticles (for more details see SI). The analysis (Fig.S3 in SI) indicates the amount of α-BGT (4.8 10^{-4} g L^{-1}) bound with SNs-COH (0.01 g L^{-1}), while the smaller amounts of α-BGT (3.8 10^{-4} g L^{-1}) are bound with SNs-COOH (0.01 g L^{-1}). The highlighted in literature intermolecular cross-linking of proteins by glutaraldehyde[21] is worth noting as a reason for the cross-linking of α-BGT into the aggregates which can admix with SNs-COH-α-BGT under their phase separations.

Luminescence of the targeted silica nanoparticles and their sensing functionality

Emission spectra of both the initial and surface decorated silica nanoparticles are manifested by four bands peculiar for Tb(III)-centered luminescence, which are 489 nm ($^5D_4 \rightarrow {}^7F_6$), 541 nm ($^5D_4 \rightarrow {}^7F_5$), 582 nm ($^5D_4 \rightarrow {}^7F_4$) and 620 nm ($^5D_4 \rightarrow {}^7F_3$) (Figs. 2a, b). The energy of the intraconfigurational 4f-4f transitions is independent on both inner- and outer-sphere environment of Tb(III) ion,[45] while the intensity of the bands is greatly affected by external conditions. In particular, our previous reports[20,46] are worth noting for highlighting the impact of well-known concentration-induced quenching[47,48] on luminescence of Tb(III)-doped nanoparticles. The luminescence data presented in Fig.2 reveal the effect of the surface decoration on intensity of the 4f-4f transitions. It is worth noting that the observed surface decoration effect on the luminescence correlates with the aggregation behavior of the decorated and the targeted silica nanoparticles. Thus, significant quenching observed for SNs-COH and their targeted analogues (SNs(COH)-α-BGT) can be explained by the concentration-induced quenching which, in turn, results from the nanoparticles aggregation (Table 1).

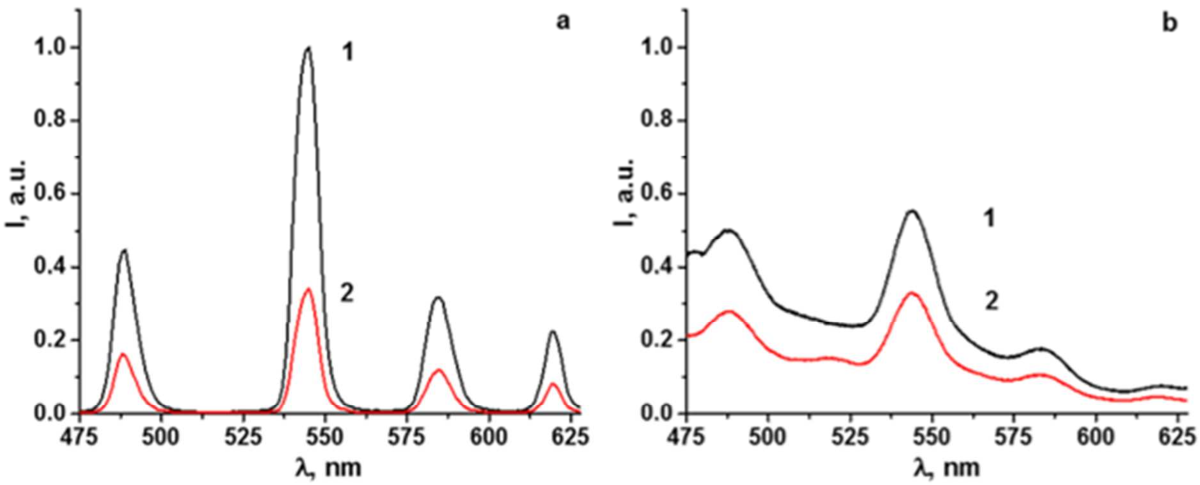

Figure 2. (a) Emission spectra of aqueous dispersion of SNs-COOH (1), SNs(COOH)-α-BGT (2) C = 0.017 g L^{-1}, slit 3/3; (b) Emission spectra of aqueous dispersion of SNs-COH (1), SNs(COH)-α-BGT (2) C = 0.01 g L^{-1}, slit 7/7, λ_{ex} = 330 nm.

The above-mentioned results point to possibility of correlation between the sensing function of the targeted silica nanoparticles and their aggregation behavior, since the latter is a reason for decreased active surface of the nanoparticles. This, in turn, can affect permeation of H^+ ions into the silica nanoparticles. The luminescence measurements of the Tb(III)-centered luminescence of SNs(COH)-α-BGT, SNs(COOH)-α-BGT and their untargeted counterparts in aqueous solutions of acetic acid were performed to reveal the quenching effect of acetic acid on the luminescence of the differently decorated nanoparticles. The quenching effect is plotted in Fig. 3 as I/I_0 (I_0 and I are the intensities of the band at 541 nm measured in the colloids before and after the acidification) versus concentration of acetic acid. Indeed, the results (Fig.3) indicate greater luminescence response of both SNs-COOH and SNs(COOH)-α-BGT to acetic acid versus SNs-COH and their targeted counterparts.

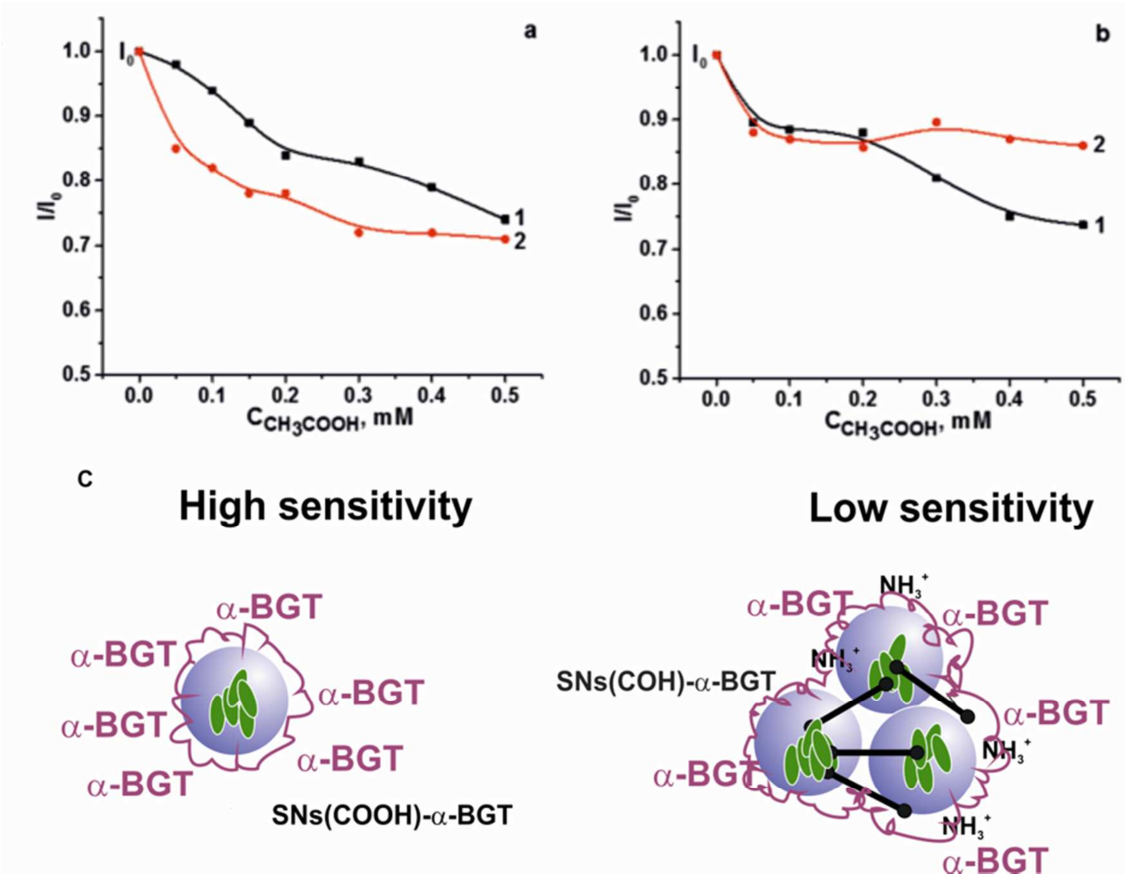

Figure 3. (a) I/I_0 values of SNs-COOH (1) (C = 0.05 g L^{-1}) and SNs(COOH)-α-BGT (2) (C = 0.017 g L^{-1}) at different concentrations of CH_3COOH; (b) I/I_0 values of SNs-COH (1) (C = 0.01 g L^{-1}) and SNs(COH)-α-BGT (2) (C = 0.01 g L^{-1}) at different concentrations of CH_3COOH, λ_{ex} = 330 nm. (c) Schematic presentation of the aggregated SNs(COH)-α-BGT with lower sensitivity to acetic acid versus SNs(COOH)-α-BGT. The black sticks designate the cross-linking of the nanoparticles by glutaraldehyde.

The presented results (Fig.3) indicate that SNs(COOH)-α-BGT are the best candidate for further application in both *in vitro* and *ex vivo* monitoring of AChE-catalyzed hydrolysis of ACh, while the sensitivity of SNs(COH)-α-BGT to acetic acid is significantly decreased by their aggregation (Figs. 3a, b). Figure 3c schematically illustrates the effect of the aggregation on sensitivity of Tb(III)-centered luminescence of the targeted nanoparticles to acetic acid.

The reliability of SNs(COOH)-α-BGT in monitoring of AChE-catalyzed hydrolysis of ACh was revealed by monitoring the changing of Tb(III)-centered luminescence in time when AChE was added to the aqueous solution of SNs(COOH)-α-BGT and ACh. The I/I_0 values measured at various time duration after the addition of AChE (Fig. 4) tend to sharp decrease within about 5-7 minutes. The decrease in I/I_0 values is followed by coming to the saturation level after ten minutes (Fig. 4). The profile of I/I_0 *versus* time (Fig.4) is very similar to the previously published profiles for the untargeted Tb(III)-doped silica nanoparticles.[17] As it has been already highlighted[17] such profile results from the inhibition of AChE in the acidified conditions produced by the enzymatic hydrolysis of ACh. Indeed, the pH value tends to decrease from 8.0 to about 6.5 after five-six minutes of the enzymatic process.

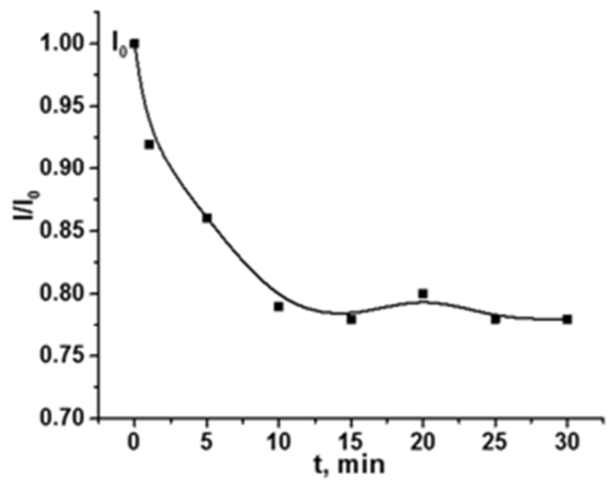

Figure 4. Time dependence of I/I_0 of SNs(COOH)-α-BGT (C = 0.034 g L^{-1}) in NaCl-based (C = 100 mM) solution of ACh (C = 0.4 mM) in the presence AChE (C = 10^{-5} mM). Initial pH is 8.0.

Ex vivo monitoring of synaptic AChE-catalyzed hydrolysis of ACh by fluorescence response of SNs(COOH)-α-BGT

Sensing of endogenous ACh hydrolysis at the neuromuscular junctions requires their selective staining by SNs(COOH)-α-BGT. The selective localization of the nanosensor, in turn, should be greatly affected by the target peptide α-BGT. Nevertheless, literature data highlight some examples of the decrease in the enzymatic activity of the proteins[24,25,27] under their covalent binding with nanoparticles. Thus, the targeting function of α-BGT can be changed due to its bioconjugation with the nanoparticles.

As it has been above mentioned incubation of the muscle samples by the dye-labelled α-BGT, Alexa 647-α-BGT, results in the efficient staining of the synaptic region which is revealed by fluorescent microscopy measurements (Figs. 5 a,b). Therefore, to reveal an impact of α-BGT in targeting of nanoparticles in synaptic region, muscles were incubated by the targeted SNs(COOH)-α-BGT or untargeted SNs(COOH) nanoparticles for ten minutes. After the washing out of the nanoparticles the analysis of fluorescence intensity in synaptic regions was performed. The efficient staining of neuromuscular junctions by SNs(COOH)-α-BGT was revealed, while the staining by SNs-(COOH) was rather poor (Figs. 5 c, d). It is also worth noting that these incubation conditions are inconvenient for detectable cellular uptake of the nanoparticles.[20] To confirm the localization of SNs(COOH)-α-BGT in the synaptic regions, we co-labeled muscles by Alexa 647-α-BGT and SNs(COOH) or SNs(COOH)-α-BGT. For this end, after incubation for ten minutes and washing out of the nanoparticles, synapses were stained by dye-labeled α-BGT. The merged fluorescent images of the synaptic regions (Fig.5 e, f) stained by both Alexa 647-α-BGT and the nanoparticles confirm localization of SNs(COOH)-α-BGT in the neuromuscular junctions. Fluorescence intensity analysis of synaptic regions showed that the staining in the case of SNs(COOH)-α-BGT was significantly brighter (a.u. = 45.2±1.7, n = 15 junctions) than staining by SNs-COOH (a.u. = 18.7±1.2, n = 17 junctions, $p < 0.001$). This result clearly indicates the impact of α-BGT in targeting of silica nanoparticles in synaptic region.

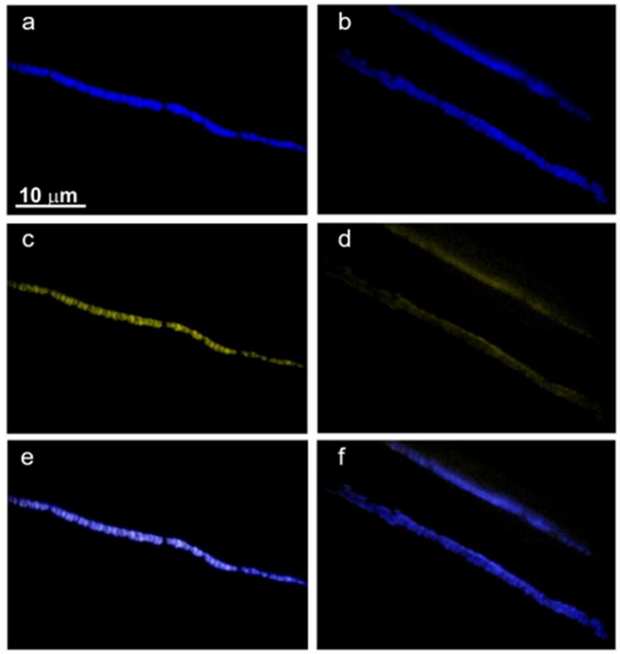

Figure 5. Fluorescent images of synaptic regions stained with Alexa 647-α-BGT (a, b) (blue), SNs(COOH)-α-BGT (c) (green) and SNs(COOH) (d) (green); (e) and (f) show merged fluorescent images of the synaptic regions stained by Alexa 647-α-BGT and SNs(COOH)-α-BGT (e) or SNs-COOH (f).

Figure 6 shows the time dependence of relative fluorescence (for more details see Experimental Section) recorded at the synaptic region of the muscle fiber. The small decline (on 4-5%) in the I/I_0 during first 5-6 min observed under basal conditions most probably reflects a photobleaching. After rest period lasted 6 min, massive release of endogenous acetylcholine from nerve terminals was evoked by intense motor nerve stimulation (3 min, 20 Hz), while the low frequency stimulation at 0.02 Hz did not alter significantly the fluorescence of the SNs (Fig. S4). The high frequency stimulation led to a sharp decrease in the fluorescence. After the end of the stimulation the fluorescence is partially recovered with more slow kinetics in the further 5 min. Application of exogenous acetylcholine (1 mM) for 3 min also produced a rapid drop in the fluorescence. Following washout of acetylcholine results in the fluorescence increase to the level before the exogenous ACh treatment within about 4-5 min (Fig. 6). No significant marked changes were reveled in the exrajunctional region of muscle fiber in response to 20 Hz or application of exogenous ACh (Fig. S5).

Additionally, the fluorescence was measured for the muscle pretreated with an irreversible inhibitor of AChE, paraoxon. This treatment completely prevented the decrease in the fluorescence induced by both endogenous and exogenous acetylcholine (Fig. 6). It should be noted that the slow decline of fluorescence was also observed in paraoxon-pretreated muscles, thus confirming a photobleaching mechanism of this phenomenon. But amplitude of these changes is significantly less compared to that in response to high-frequency stimulation or ACh application.

Altogether, these data argue for the monitoring of AChE-catalyzed hydrolysis of ACh in the neuromuscular junctions by the fluorescence intensity of SNs(COOH)-α-BGT.

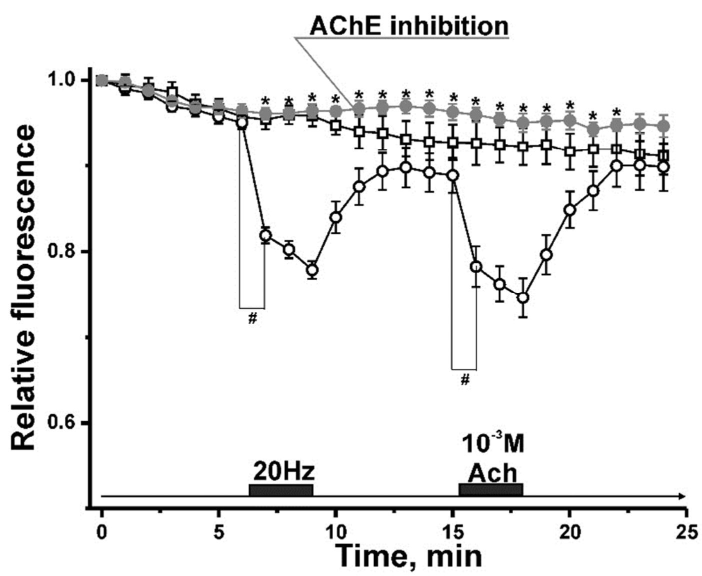

Figure 6. Time dependence of relative fluorescence (I/I_0) measured in synaptic region by fluorescent microscopy for the muscle samples exposed to the SNs (open circles, n = 7), the similar values measured for the muscles pretreated by paraoxon are represented by dark circles

(n = 6). Effects of the motor nerve stimulation with high-frequency and the exogenous ACh on the fluorescence of the SNs are designated by horizontal boxes. Baseline control (without the stimulation or inhibition of AChE, n = 4) is indicated by open squares.

CONCLUSIONS

Summarizing, luminescent Tb(III)-doped silica nanoparticles targeted by α-bungarotoxin are for the first time introduced as nanosensors for luminescent monitoring of acetylcholinesterase (AChE)-catalyzed hydrolysis of endogenous acetylcholine (ACh) released at the neuromuscular junctions of isolated muscles. The sensing function of the nanosensors results from the quenching of Tb(III)-centered luminescence due to proton-induced degradation of luminescent Tb(III) complexes doped into silica nanoparticles (23 nm), when acetic acid is produced from the enzymatic hydrolysis of ACh. The optimal synthetic procedure for the targeting of the nanosensor by α-bungarotoxin without loss of its sensing function to acetic acid produced by AChE-catalyzed hydrolysis of ACh was developed. The selective staining of neuromuscular junctions by optimal targeted nanosensor was revealed. The *ex vivo* fluorescence microscopy measurements highlighted the sensing reliability of AChE-catalyzed hydrolysis of ACh at the neuromuscular junctions by the fluorescence intensity of the nanosensor targeted by α-bungarotoxin.

ASSOCIATED CONTENT

Supporting Information. Experimental section, TEM images of nanoparticles and the determination of amino-groups quantity on silica surface by fluorescamine-based procedure are presented in Supporting Information.

AUTHOR INFORMATION

Corresponding Author

* E-mail: alsu_mukhamet@mail.ru

ACKNOWLEDGMENT

This work in part of synthesis and characterization of the nanomaterial was supported by Russian Science Foundation grant no.14-50-00014 awarded to A.R.M., S.V.F., K.A.P., A.R.M and O.G.S.

REFERENCES

(1) Kawada, T.; Akiyama, T.; Shimizu, S.; Kamiya, A.; Uemura, K.; Li, M.; Shirai, M.; Sugimachi, M. Detection of endogenous acetylcholine release during brief ischemia in the rabbit ventricle: A possible trigger for ischemic preconditioning. *Life Sci.* **2009**, *85*, 597–601.

(2) Consolo, S.; Wu, C. F.; Fiorentini, F.; Ladinsky, H.; Vezzani, A. Determination of Endogenous Acetylcholine Release in Freely Moving Rats by Transstriatal Dialysis Coupled to a Radioenzymatic Assay: Effect of Drugs. *J. Neurochem*. **1987**, *48*, 1459–1465.

(3) Fan, W.; Zhang, Z. Determination of acetylcholine and choline in rat brain tissue by FIA with immobilized enzymes and chemiluminescence detection. *Microchem. J.* **1996**, *53*, 290–295.

(4) Liu, Y.; Erdman, A. G.; Cui, T. Acetylcholine biosensors based on layer-by-layer self-assembled polymer/nanoparticle ion-sensitive field-effect transistors. *Sens. Actuators, A* **2007**, *136*, 540–545.

(5) Aynaci, E.; Yaşar, A.; Arslan, F. An amperometric biosensor for acetylcholine determination prepared from acetylcholinesterase-choline oxidase immobilized in polypyrrole-polyvinylsulpfonate film. *Sens. Actuators, B* **2014**, *202*, 1028–1036.

(6) Kanik, F. E.; Kolb, M.; Timur, S.; Bahadir, M.; Toppare, L. An amperometric acetylcholine biosensor based on a conducting polymer. *Int. J. Biol. Macromol.* **2013**, *59*, 111–118.

(7) Asri, R.; O'Neill, B.; Patel, J. C.; Siletti, K. A.; Rice, M. E. Detection of evoked acetylcholine release in mouse brain slices. *Analyst* **2016**, *141*, 6416–6421.

(8) Baker, K. L.; Bolger, F. B.; Lowry, J. P. Development of a microelectrochemical biosensor for the real-time detection of choline. *Sens. Actuators, B* **2017**, *243*, 412–420.

(9) Goyal, R. K.; Chaudhury, A. Structure activity relationship of synaptic and junctional neurotransmission. *Auton. Neurosci.* **2013**, *176*, 11–31.

(10) Scimemi, A.; Beato, M. Determining the neurotransmitter concentration profile at active synapses. *Mol. Neurobiol.* **2009**, *40*, 289–306.

(11) Dai, N.; Kool, E. T. Fluorescent DNA-based enzyme sensors. *Chem. Soc. Rev.* **2011**, *40*, 5756–5770.

(12) Arruda, I. G.; Guimarães, F. E. G.; Ramos, R. J.; Vieira, N. C. S. Self-assembly of SiO_2nanoparticles for the potentiometric detection of neurotransmitter acetylcholine and its inhibitor. *J. Nanosci. Nanotechnol*. **2014**, *14*, 6658–6661.

(13) Chauhan, N.; Narang, J.; Jain, U. Highly sensitive and rapid detection of acetylcholine using an ITO plate modified with platinum-graphene nanoparticles. *Analyst* **2015**, *140*, 1988–1994.

(14) Chauhan, N.; Chawla, S.; Pundir, C.S.; Jain, U. An electrochemical sensor for detection of neurotransmitter-acetylcholine using metal nanoparticles, 2D material and conducting polymer modified electrode. *Biosens. Bioelectron*. **2017**, *89*, 377–383.

(15) Li, H.; Guo, Y.; Xiao, L.; Chen, B. A fluorometric biosensor based on H2O2-sensitive nanoclusters for the detection of acetylcholine. *Biosens. Bioelectron*. **2014**, *59*, 289–292.

(16) Walsh, R.; Morales, J. M.; Skipwith, C. G.; Ruckh, T. T.; Clark, H. A. Enzyme-linked DNA dendrimer nanosensors for acetylcholine. *Sci. Rep.* **2015**, DOI:10.1038/srep14832.

(17) Mukhametshina, A. R.; Fedorenko, S. V.; Zueva, I. V.; Petrov, K. A.; Masson, P.; Nizameev, I. R.; Mustafina, A. R.; Sinyashin, O. G. Luminescent silica nanoparticles for sensing acetylcholinesterase-catalyzed hydrolysis of acetylcholine. *Biosens. Bioelectron.* **2016**, *77*, 871–878.

(18) Mukhametshina, A.; Petrov, A.; Fedorenko, S.; Petrov, K.; Nizameev, I.; Mustafina, A.; Sinyashin, O. Luminescent nanoparticles for rapid monitoring of endogenous acetylcholine release in mice atria. *Luminescence* **2018**, DOI: 10.1002/bio.3450.

(19) Mukhametshina, A. R.; Mustafina, A. R.; Davydov, N. A.; Fedorenko, S. V.; Nizameev, I. R.; Kadirov, M. K.; Gorbatchuk, V. V.; Konovalov, A. I. Tb(III)-doped silica nanoparticles for sensing: Effect of interfacial interactions on substrate-induced luminescent response. *Langmuir* **2015**, *31*, 611–619.

(20) Fedorenko, S. V.; Mustafina, A. R.; Mukhametshina, A. R.; Jilkin, M. E.; Mukhametzyanov, T. A.; Solovieva, A. O.; Pozmogova, T. N.; Shestopalova, L. V.; Shestopalov, M. A.; Kholin, K. V.; Osin, Y. N.; Sinyashin, O. G. Cellular imaging by green luminescence of Tb(III)-doped aminomodified silica nanoparticles. *Mater. Sci. Eng., C* **2017**, *76*, 551–558.

(21) Barbosa, O.,;Ortiz, C.; Berenguer-Murcia, A.; Torres, R.; Rodrigues, R. C.; Fernandez-Lafuente, R. Glutaraldehyde in bio-catalysts design: A useful crosslinker and a versatile tool in enzyme immobilization. *RSC Adv*. **2014**, *4*, 1583–1600.

(22) Cho, H. J.; Jang, W. J.; Moon, S. Y.; Lee, J. M.; Kim, J.-H.; Han, H.-S.; Kim, K.-W.; Lee, B.-J.; Kong, I.-S. Immobilization of β-1,3-1,4-glucanase from Bacillus sp. on porous silica for production of β-glucooligosaccharides. *Enzyme Microb. Technol.* **2018**, *110*, 30–37.

(23) Vazquez-Ortega, P. G.; Alcaraz-Fructuoso, M. T.; Rojas-Contreras, J. A.; López-Miranda, J.; Fernandez-Lafuente, R. Stabilization of dimeric β-glucosidase from Aspergillus niger via glutaraldehyde immobilization under different conditions. *Enzyme Microb. Technol.* **2018**, *110*, 38–45.

(24) Al-Dhrub, A. H. A.; Sahin, S.; Ozmen, I.; Tunca, E.; Bulbul, M. Immobilization and characterization of human carbonic anhydrase I on amine functionalized magnetic nanoparticles. *Process Biochem*. **2017**, *57*, 95–104.

(25) Feng, J.; Yu, S.; Li, J.; Mo, T.; Li, P. Enhancement of the catalytic activity and stability of immobilized aminoacylase using modified magnetic Fe_3O_4 nanoparticles. *Chem. Eng. J.* **2016**, *286*, 216–222.

(26) Goftman, V. V.; Aubert, T.; Ginste, D. V.; Van Deun, R.; Beloglazova, N. V.; Hens, Z.; De Saeger, S.; Goryacheva, I. Y. Synthesis, modification, bioconjugation of silica coated fluorescent quantum dots and their application for mycotoxin detection. *Biosens. Bioelectron.* *2016*, *79*, 476–481.

(27) Qi, H.; Du, Y.; Hu, G.; Zhang, L. Poly(carboxybetaine methacrylate)-functionalized magnetic composite particles: A biofriendly support for lipase immobilization. *Int. J. Biol. Macromol*. **2018**, *107*, 2660–2666.

(28) Žuža, M. G.; Milašinović, N. Z.; Jonović, M. M.; Jovanović, J. R.; Kalagasidis Krušić, M. T.; Bugarski, B. M.; Knežević-Jugović, Z. D. Design and characterization of alcalase–chitosan conjugates as potential biocatalysts. *Bioprocess Biosyst. Eng*. **2017**, *40*, 1713–1723.

(29) Hermanson, G. T. Bioconjugate Techniques (Third edition); Hermanson, G. T., Eds.; Elsevier: Rockford, IL, 2013; Chapter 14, pp 549–587.

(30) Bartczak, D.; Kanaras, A. G. Preparation of peptide-functionalized gold nanoparticles using one pot EDC/Sulfo-NHS coupling, *Langmuir* **2011**, *27*, 10119–10123.

(31) Knopp, D.; Tang, D.; Niessner, R. Review: Bioanalytical applications of biomolecule-functionalized nanometer-sized doped silica particles. *Anal. Chim. Acta* **2009**, *647*, 14–30.

(32) Depalo, N.; Corricelli, M.; De Paola, I.; Valente, G.; Iacobazzi, R. M.; Altamura, E.; Debellis, D.; Comegna, D.; Fanizza, E.; Denora, N.; Laquintana, V.; Mavelli, F.; Striccoli, M.; Saviano, M.; Agostiano, A.; Del Gatto, A.; Zaccaro, L.; Curri, M. L. NIR Emitting Nanoprobes Based on Cyclic RGD Motif Conjugated PbS Quantum Dots for Integrin-Targeted Optical Bioimaging. *ACS Appl. Mater. Interfaces* **2017**, *9*, 43113–43126

(33) Sapsford, K. E.; Algar, W. R.; Berti, L.; Gemmill, K. B.; Casey, B. J.; Oh, E.; Stewart, M. H.; Medintz, I. L. Functionalizing nanoparticles with biological molecules: Developing chemistries that facilitate nanotechnology. *Chem. Rev.* **2013**, *113*, 1904–2074.

(34) Schiestel, T.; Brunner, H.; Tovar, G. E. M. Controlled surface functionalization of silica nanospheres by covalent conjugation reactions and preparation of high density streptavidin nanoparticles. *J. Nanosci. Nanotechnol*. **2004**, *4*, 504–511.

(35) Taylor, A., Krupskaya, Y., Costa, S., Oswald, S., Kramer, K., Füssel, S., Klingeler, R., Büchner, B., Borowiak-Palen, E., Wirth, M.P. Functionalization of carbon encapsulated iron nanoparticles. *J. Nanopart. Res*. **2010**, *12*, 513–519.

(36) Hu, Z.; Tan, J.; Lai, Z.; Zheng, R.; Zhong, J.; Wang, Y.; Li, X.; Yang, N.; Li, J.; Yang, W.; Huang, Y.; Zhao, Y.; Lu, X. Aptamer Combined with Fluorescent Silica Nanoparticles for Detection of Hepatoma Cells. *Nanoscale Res. Lett*. **2017**, *12*, 96.

(37) Montalti, M.; Prodi, L.; Rampazzo, E.; Zaccheroni, N. Dye-doped silica nanoparticles as luminescent organized systems for nanomedicine. *Chem. Soc. Rev*. **2014**, *43*, 4243–4268.

(38) Moura, C. C.; Segundo, M. A.; das Neves, J.; Reis, S.; Sarmento, B. Co-association of methotrexate and SPIONs into anti-CD64 antibody-conjugated PLGA nanoparticles for theranostic application. *Int. J. Nanomed*. **2004**, *9*, 4911–4922.

(39) Treerattrakoon, K.; Chanthima, W.; Apiwat, C.; Dharakul, T.; Bamrungsap, S. Oriented conjugation of antibodies against the epithelial cell adhesion molecule on fluorescently doped silica nanoparticles for flow-cytometric determination and in vivo imaging of EpCAM, a biomarker for colorectal cancer. *Microchim. Acta* **2017**, *184*, 1941–1950.

(40) Tan, J.; Yang, N.; Hu, Z.; Su, J.; Zhong, J.; Yang, Y.; Yu, Y.; Zhu, J.; Xue, D.; Huang, Y.; Lai, Z.; Huang, Y.; Lu, X.; Zhao, Y. Aptamer-Functionalized Fluorescent Silica Nanoparticles for Highly Sensitive Detection of Leukemia Cells. *Nanoscale Res. Lett.* **2016**, *11*, 298.

(41) Keleştemur, S.; Altunbek, M.; Culha, M. Influence of EDC/NHS coupling chemistry on stability and cytotoxicity of ZnO nanoparticles modified with proteins. *Appl. Surf. Sci.* **2017**, *403*, 455–463.

(42) Chen, Z.-Z.; Cai, L.; Dong, X.-M.; Tang, H.-W.; Pang, D.-W. Covalent conjugation of avidin with dye-doped silica nanopaticles and preparation of high density avidin nanoparticles as photostable bioprobes. *Biosens. Bioelectron*. **2012**, *37*, 75–81

(43) Chen, Y.; Zhang, Y. Fluorescent quantification of amino groups on silica nanoparticle surfaces. *Anal. Bioanal. Chem*. **2011**, *399*, 2503–2509.

(44) Udenfriend, S.; Stein, S.; Böhlen, P.; Dairman, W.; Leimgruber, W.; Weigele, M. Fluorescamine: A reagent for assay of amino acids, peptides, proteins, and primary amines in the picomole range. *Science* **1972**, *178*, 871–872.

(45) Eliseeva, S. V.; Bünzli, J.-C. G. Lanthanide luminescence for functional materials and bio-sciences. *Chem. Soc. Rev*. **2010**, *39*, 189−227.

(46) Zairov, R.; Mustafina, A.; Shamsutdinova, N.; Nizameev, I.; Moreira, B.; Sudakova, S.; Podyachev, S.; Fattakhova, A.; Safina, G.; Lundstrom, I.; Gubaidullin, A.; Vomiero, A. High performance magneto-fluorescent nanoparticles assembled from terbium and gadolinium 1,3-diketones. *Sci. Rep*. **2017**, *7*, 40486.

(47) Zhao, C.-J.; Cai, J.-L.; Li, R.-Y.; Tie, S.-L.; Wan, X.; Shen, J.-Y. White light emission from Eu^{3+}/Tb^{3+}/Tm^{3+} triply-doped aluminoborate glass excited by UV light. *J. Non-Cryst. Solids* **2012**, *358*, 604−608.

(48) Su, Q.; Han, S.; Xie, X.; Zhu, H.; Chen, H.; Chen, C.-K.; Liu, R.-S.; Chen, X.; Wang, F.; Liu, X. The Effect of Surface Coating on Energy Migration-Mediated Upconversion. *J. Am. Chem. Soc*. **2012**, *134*, 20849−20857.

Graphical abstract

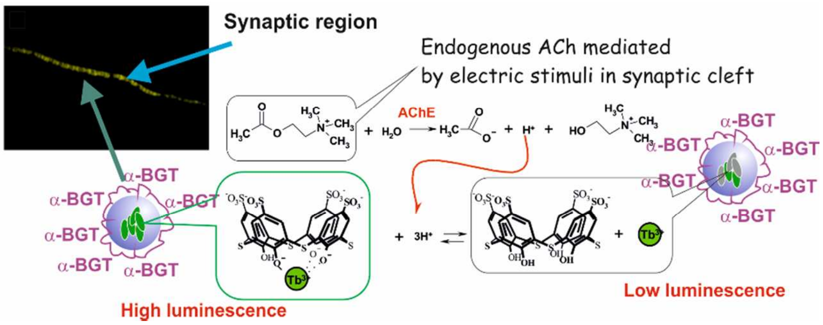

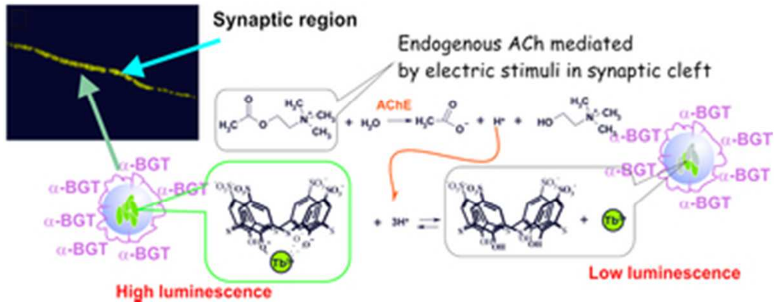

Graphical abstract

32x12mm (300 x 300 DPI)

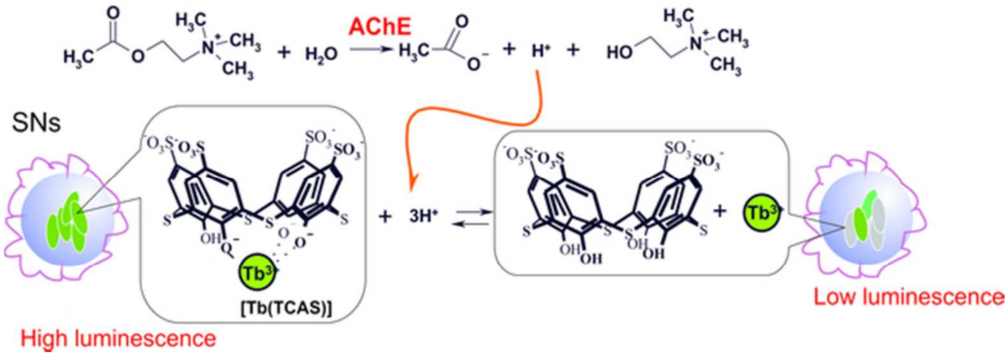

Scheme 1

55x19mm (300 x 300 DPI)

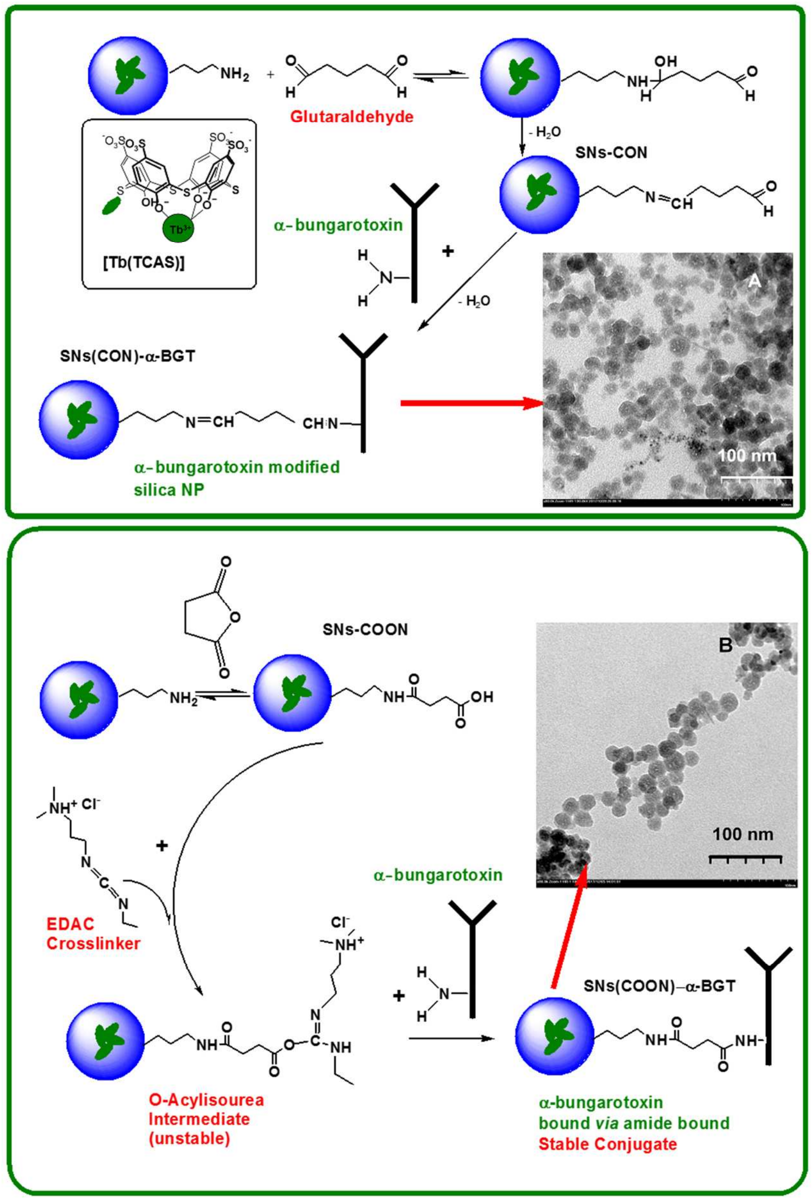

Figure 1

165x244mm (150 x 150 DPI)

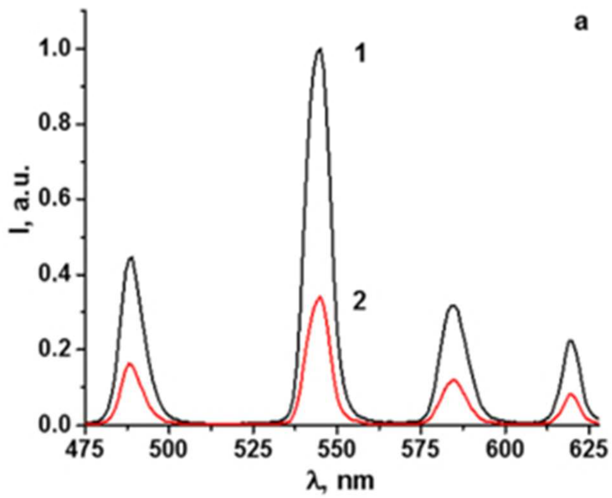

Figure 2a

82x67mm (96 x 96 DPI)

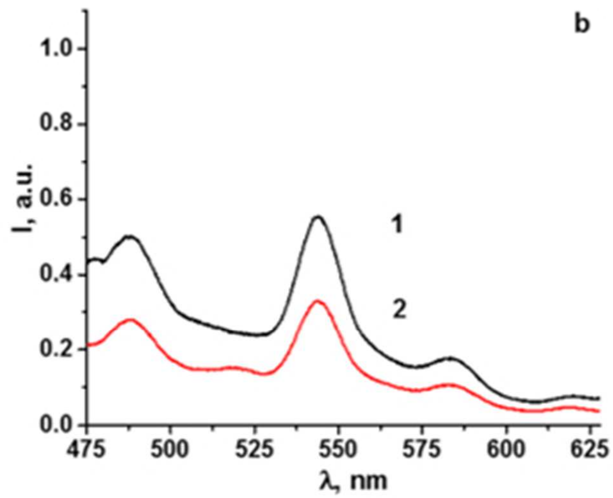

Figure 2b

82x67mm (96 x 96 DPI)

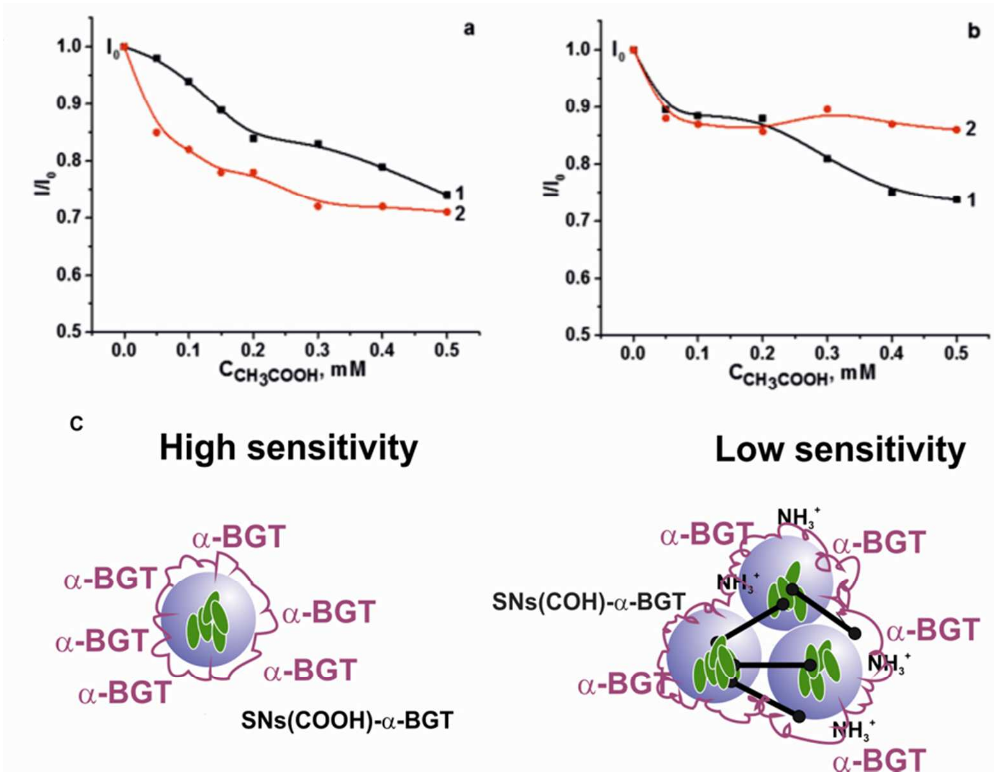

Figure 3

160x122mm (150 x 150 DPI)

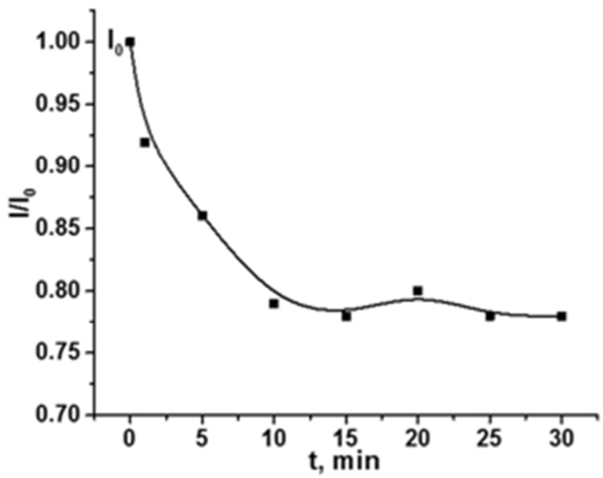

Figure 4

81x64mm (96 x 96 DPI)

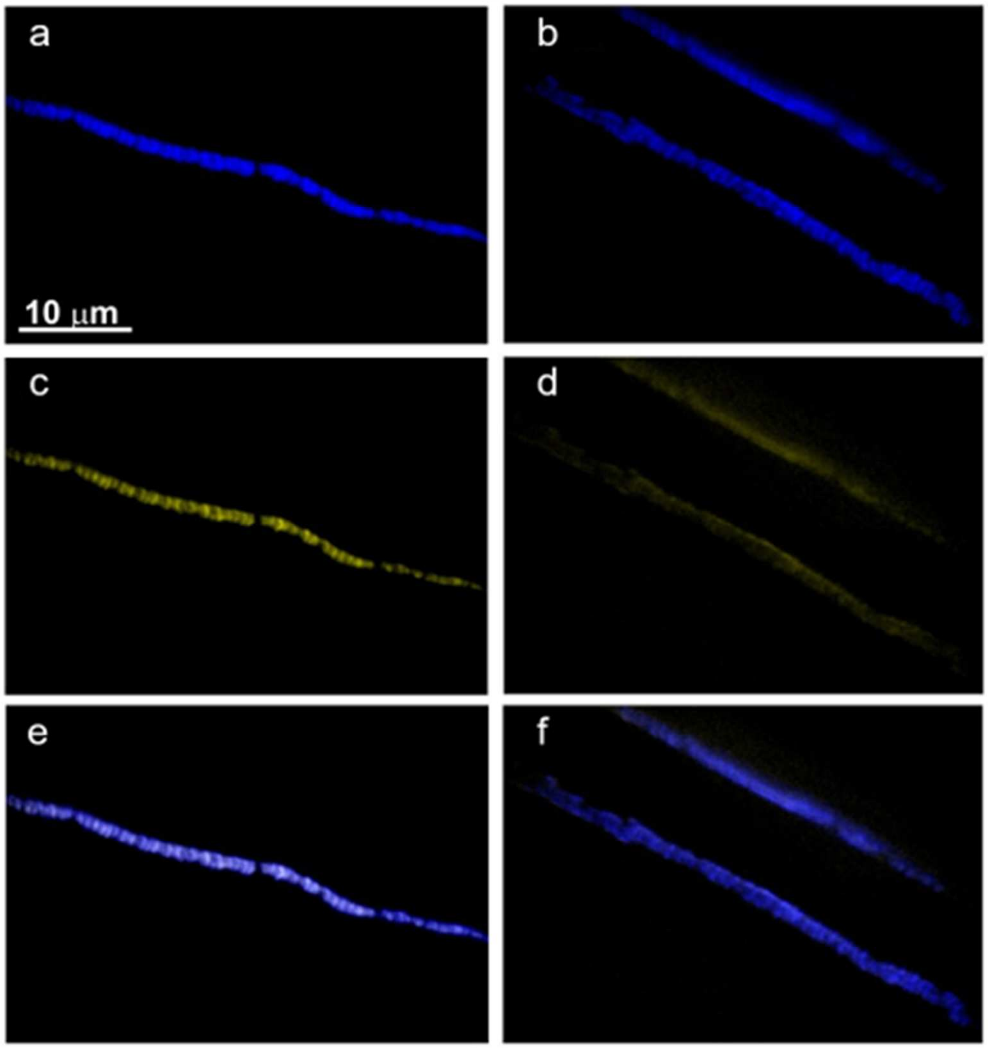

Fidure 5

84x89mm (149 x 149 DPI)

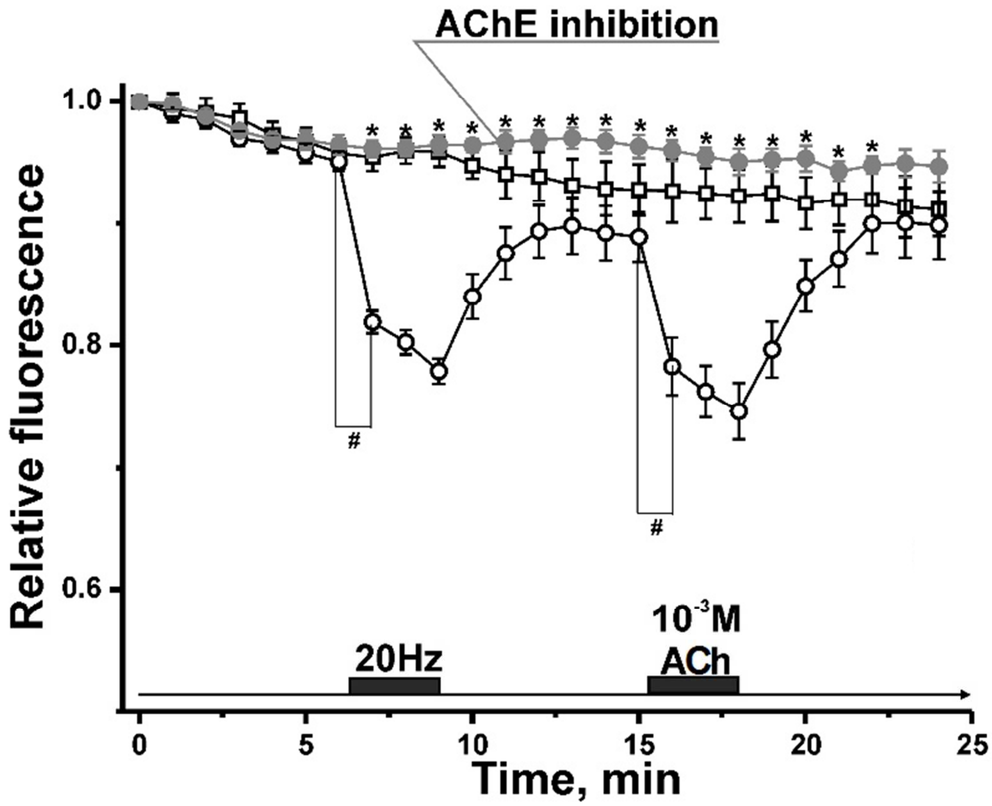

Figure 6

92x75mm (220 x 220 DPI)